

A hybrid Eulerian-Lagrangian Vlasov method for nonlinear wave-particle interaction in weakly inhomogeneous magnetic field

Jiangshan Zheng^a, Ge Wang^b, Bo Li^a

^aSchool of Physics, Beihang University, Beijing, Beijing 100191, China

^bInstitute for Fusion Studies, The University of Texas, Austin, Texas, 78712, USA

Abstract

We present a hybrid Eulerian-Lagrangian Vlasov solver for nonlinear resonant wave-particle interactions problems in weakly inhomogeneous magnetic field. The governing Vlasov equation is derived from a recently proposed resonance tracking Hamiltonian method. The method tracks the dynamics of deeply trapped resonant particles in a coherent wave. It gives the evolution of the distribution function with a scale separated Hamiltonian that containing the slowly-varying motion about the resonant frame of reference and fast-varying coherent interactions. The hybrid method solves the slowly-varying phase space dynamics by Lagrangian method along the resonant trajectory, while simultaneously manages the fast-varying phase-space evolution in Eulerian grid with an adaptive time step interpolated differential operator scheme. We apply our method to study the frequency chirping problem of whistler mode chorus wave in the Earth magnetosphere and successfully reproduce the chirping chorus wave. The results in well agree with previous research. With a focus on nonlinear resonant wave-particle interaction in the weakly inhomogeneous regime, our approach can give high resolution for the fast varying phase space at low computational cost. It could provide additional insights of the wave instabilities and particle energy transfer compared to the conventional Vlasov and particle-in-cell methods.

1. Introduction

Wave-particle interaction, especially the nonlinear resonant interaction, is of great importance and have been extensively discussed in a broad spectrum of plasma physics. In magnetically confined fusion devices, there have Alfvén wave instabilities [1, 2] which are associated with mode frequency sweeping and lead to premature ejection of alpha particles that deteriorate plasma confinement [3]. In the planetary magnetosphere [4], as well as in the laboratory devices [5, 6], researchers have studied the chorus wave, which is associated with various geophysical activity like relativistic electron precipitation, X-ray microbursts, pulsating and diffuse auroras [7, 8, 9]. It has been demonstrated that the nonlinear resonant interaction between toroidal Alfvén eigenmodes and fusion-born alpha particles, the energetic electrons and the whistler-mode wave play the key role in these nonlinear instabilities, and therefore it is greatly concerned to build solid and various theoretical descriptions and numerical models to further discuss these wave-particle interactions.

In general, the wave-particle interactions can be described by the Vlasov equation and self-consistently coupled with the wave evolution. In the homogeneous plasmas [10, 11] or in the nonuniform regime with spatial symmetry [12, 13, 14], the involved wave can be treated as standing wave with stationary fixed wavenumber or mode number. In such cases, the interactions are confined to the periodical localized regions. Consequently, kinetic simulations in these scenarios become notably straightforward, benefiting from the inherent periodicity of the system. These simulations primarily entail the examination of momentum space within a local spatial volume, effectively addressing a single-scale wave-particle interaction problem, thus rendering them highly amenable to numerical solutions.

However, when dealing with inhomogeneous scenarios where periodicity no longer holds, the complexity significantly escalates. Even weak inhomogeneity can break the periodicity and significantly modify the nonlinear wave-particle interaction. The nonuniform spatial dependence brings extra dimensions on both the wave evolution and the fine structures of resonance particle phase space. The interaction have to be considered on the whole domain instead of in a single spatial volume. Although, techniques like WKB approximation [15] or slowly varying envelope approximation [16] can be applied to simplify the wave calculation, it is challenging to find a suitable approach to split the scales of the resonant particles due to intricate wave-particle interactions along the inhomogeneous magnetic field. Consequently, the rapidly changing temporal and spatial scales come into play across all dimensions of the resonant particle phase space, resulting in a significantly heavier computational workload than in homogeneous plasma settings. Also, it becomes clear that traditional methods lack the required precision to describe the nuanced behavior of particles subjected to the nonlinearity imposed by inhomogeneous magnetic fields and chirping waves.

To address these limitations, people make efforts to decouple the multiple scale of motion to get a reduced description of the system. For the whistler wave packet propagate in a one dimensional weakly inhomogeneous magnetic field, Karpman et al. [17] have proposed reduced Vlasov theory in which new integral of motion for the resonant particle is obtained, and therefore degenerating the original system. In our recent work [], we have proposed a novel theoretical framework that redefines the physics within reference frames moving at

local resonant velocities. We transcend the stationary phase approximation [18, 19], and expand the wave phase about the local resonance center, which effectively decoupling the motion scales. This results in the formulation of a new Hamiltonian represented in novel canonical coordinates and momenta. The Hamiltonian can be divided into two distinct subspaces, which is similar to Karpman’s work but considers self-consistently the variation of both wave number and frequency. The one is ξ, Ω space, corresponding to the fast-varying wave particle interaction terms. The other is ϑ, \mathcal{J} space, corresponding to the slowly-varying one seen by the resonance frame moving along the resonance trajectory. The particle slowly varying scale corresponds to the characteristic length of background plasma inhomogeneity, and the dynamics in ξ, Ω subspace can be treated as quasi-periodical in ξ dimension, similar to the behavior in homogeneous plasma settings. Based on previous analysis, we formulate the corresponding Vlasov equation for the resonance particle distribution function $f(t, s_i, \vartheta, \mathcal{J}, \xi, \Omega)$. The equation is readily constructed as an advective form of two separated Hamiltonian flows and the advective term of reference frame moving along resonance trajectories.

$$\frac{\partial f}{\partial t} + \frac{ds_i}{dt} \frac{\partial f}{\partial s_i} + [f, H]_{\vartheta, \mathcal{J}} + [f, H]_{\xi, \Omega} = 0, \quad (1)$$

where the bracket is the canonical Poisson bracket.

The above Vlasov equation consists of two separated motions, each of which is solved individually using a hybrid method. Here we consider a delta f Vlasov solver based on an elaborated hybrid Eulerian-Lagrangian (HEL) method for solving system of this general form [20]. The Vlasov system is coupled to the slowly varying wave envelope equation in the resonance frame. In our numerical scheme, the entire system is solved through a series of four distinct steps. Firstly, we apply a conservative form Interpolated Differential Operator (IDO-CF) method to the Eulerian grid to solve the evolution in ξ, Ω domain, it provides high resolution, allowing us to identify and track the formation and evolution of resonant structures arising from the rapidly changing wave-particle interactions. Secondly, the perturbed current is then integrated from the perturbed distribution function with local equilibrium quantities. Thirdly, the trajectory of Lagrangian markers sampled in slowly varying domain are solved by Runge-Kutta (RK) method. Subsequently, we update the perturbed distribution on the new marker coordinates. It’s worth noting that we employ an adaptive time step RK solver in the Eulerian part to bridge the gap in time steps between the ξ, Ω and $s, \vartheta, \mathcal{J}$ domains. Finally, after completing the particle solver, we couple the current to the wave equation and evolve the wave to the next time step. We derive both first and second-order wave equation forms, which we solve using the RK method and an implicit upwind scheme.

We use the frequency chirping phenomenon of whistler wave in the Earth magnetosphere as benchmark. The results obtained provide the linear growth rate, which aligns closely with theoretical predictions, validating the accuracy of our simulations. Additionally, we present the presence of trapped particle phase space holes and compare them with the theoretical results, further affirming the robustness of our simulation, even at the nonlinear stage. By incorporating advanced numerical techniques and a more comprehensive understanding

of the magnetic field variations, we endeavor to uncover the elusive fine structure of resonant particles. This endeavor holds the potential to revolutionize our comprehension of the intricate interplay between waves and particles within inhomogeneous magnetic fields.

We organized our paper as follows. In section 2, we present the HEL theory for our scale separated Vlasov system and introduce the IDO-CF numerical scheme. In section 3, we present the details of the numerical modeling on the wave slowly varying envelope. Section 4 provides a detailed description on our code design and implementations. Finally, the conclusion is provided in section 5.

2. The Hybrid Eulerian-Lagrangian Solver for the Vlasov system

Consider the delta f form of Vlasov system in equation (1). The evolution of perturbed distribution function $\delta f(\vartheta, \mathcal{J}; \xi, \Omega; s, t)$ is

$$\frac{\partial \delta f}{\partial t} + \frac{ds}{dt} \frac{\partial \delta f}{\partial s} + [\delta f, H]_{\vartheta, \mathcal{J}} + [\delta f, H]_{\xi, \Omega} = \mathcal{S}, \quad (2)$$

where the Poisson brackets are defined as

$$[f, g]_{x,y} = \frac{\partial f}{\partial x} \frac{\partial g}{\partial y} - \frac{\partial f}{\partial y} \frac{\partial g}{\partial x}. \quad (3)$$

Here ξ, Ω and ϑ, \mathcal{J} are the canonical variables corresponding to the fast and slowly varying scales, respectively. The source term $\mathcal{S} = -[f_0, \delta H]_{\vartheta, \mathcal{J}} - [f_0, \delta H]_{\xi, \Omega}$ where f_0 is the equilibrium distribution function and δH denotes the perturbed Hamiltonian due to the resonant wave-particle interactions. Note that the derivatives of δH with respect to the slowly varying coordinates ϑ and \mathcal{J} can be neglected due to the separation of perturbation and equilibrium scales. Besides, $\partial f_0 / \partial \xi$ is vanished since f_0 does not generally depend on the fast varying angle coordinate ξ . Thus, the source term can be simplified as

$$\mathcal{S} = \frac{\partial \delta H}{\partial \xi} \frac{\partial f_0}{\partial \Omega}. \quad (4)$$

The variation of the angular coordinate ϑ is negligible, owing to the weakly inhomogeneous nature of the plasmas, while the dynamics of \mathcal{J}, Ω , and ξ remain entirely unaffected by ϑ . Therefore we neglect the term $\dot{\vartheta}$ in the Vlasov equation and the Poisson bracket becomes

$$[\delta f, H]_{\vartheta, \mathcal{J}} \simeq -\dot{\mathcal{J}} \frac{\partial \delta f}{\partial \mathcal{J}} \quad (5)$$

where the dot denotes the time derivative.

We now implement the hybrid method to solve the Vlasov system, which has been structured to separate the fast and slowly varying scales within the Hamiltonian theory. We utilize the Eulerian method to model the fast-varying phase space ξ, Ω and employ the Lagrangian method to model the slowly varying coordinates \mathcal{J} and the resonance frame coordinate s . The distribution function is written as [20]

$$\delta f(\xi, \Omega, \mathcal{J}, s, t) = \sum_{k,l} g_{k,l}(t, \xi, \Omega) \delta(s - s_k(t), \mathcal{J} - \mathcal{J}_l), \quad (6)$$

where $g_{k,l}(t, \xi, \Omega)$ represents the distribution function in ξ, Ω space with k and l denoting the indices of the Lagrangian markers. Then the evolution equation for $g_{k,l}(t, \xi, \Omega)$ for each marker labeled by k and l is

$$\frac{\partial g}{\partial t} + [g, H]_{\xi, \Omega} = \mathcal{S} . \quad (7)$$

Here we omit the index k and l of g for convenience.

In the Lagrangian step, it is essential for the marker to move in tandem with the resonance frame throughout the spatial domain, i.e.,

$$\dot{s}_k = v_r(s_k(t)) , \quad (8)$$

where v_r is the resonant velocity. The motion equation for slowly varying coordinate \mathcal{J} is

$$\dot{\mathcal{J}} = [\mathcal{J}, H]_{\theta, \mathcal{J}} . \quad (9)$$

2.1. The Eulerian step

Now we solve the fast-varying phase space dynamics for each Lagrangian at s_k, \mathcal{J}_l . For the numerical treatment, the Vlasov equation (7) is expressed as

$$\frac{\partial g}{\partial t} + m \frac{\partial g}{\partial \xi} - n \frac{\partial g}{\partial \Omega} = \mathcal{S} , \quad (10)$$

where

$$m(\xi, \Omega) = \frac{\partial H}{\partial \Omega}, \quad n(\xi, \Omega) = \frac{\partial H}{\partial \xi} . \quad (11)$$

To achieve high-order accuracy, we apply the IDO method [21] to solve the 2D Vlasov equation in ξ, Ω domain. The IDO scheme applies the polynomial as local interpolation functions to replace the distributions along each coordinate in phase space. Here a second-order polynomial is used as interpolation stencil for a function $g(x)$ from x_i to x_{i+1} ,

$$G(x, g_i, g_{i+1}, \sigma_{i+\frac{1}{2}}) = a(x - x_i)^2 + b(x - x_i) + c , \quad (12)$$

where $g_i \equiv g(x_i)$, $g_{i+1} \equiv g(x_{i+1})$ are function values on the grid, and $\sigma_{i+\frac{1}{2}}$ is the cell integral value

$$\sigma_{i+\frac{1}{2}} \equiv \int_{x_i}^{x_{i+1}} g(x) \, dx , \quad (13)$$

and the coefficients are determined from the grid value and the line integral over the cell,

$$\begin{aligned} a &= \frac{3(g_i + g_{i+1})}{\Delta x^2} - \frac{6\sigma_{i+\frac{1}{2}}}{\Delta x^3} , \\ b &= -\frac{2(2g_i + g_{i+1})}{\Delta x} + \frac{6\sigma_{i+\frac{1}{2}}}{\Delta x^2} , \\ c &= g_i . \end{aligned} \quad (14)$$

For equation (10), the derivatives of g with respect to ξ and Ω are numerically represented by the interpolating stencil introduced above. The discretized form of the Vlasov equation becomes,

$$\begin{aligned} \left. \frac{\partial g}{\partial t} \right|_{i,j} &= -m_{i,j} \left. \frac{\partial}{\partial \xi} G(\xi; g_{i,j}, g_{i+1,j}, \rho_{i+\frac{1}{2},j}) \right|_{i,j} \\ &\quad + n_{i,j} \left. \frac{\partial}{\partial \Omega} G(\Omega; g_{i,j}, g_{i,j+1}, \kappa_{i,j+\frac{1}{2}}) \right|_{i,j} \\ &\quad + \mathcal{S}_{i,j}, \end{aligned} \quad (15)$$

where i and j are the grid index for ξ and Ω , respectively. The grid and the sampling points are demonstrated in Fig. 1.

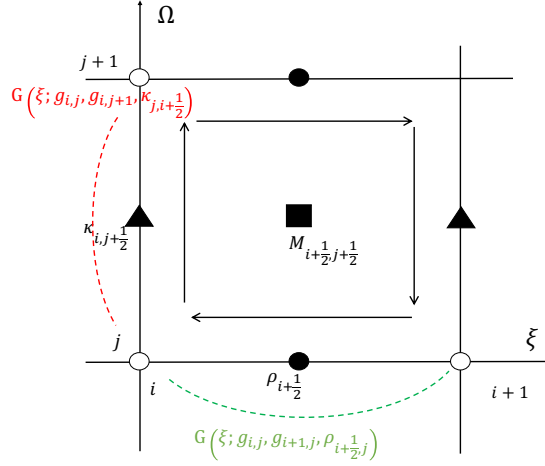


Figure 1: The interpolating functions and cell integrated values in ξ, Ω domain.

The interpolation relies on the line integrated values $\rho_{i+\frac{1}{2},j} = \int_{\xi_i}^{\xi_{i+1}} g_j(\xi) d\xi$ and $\kappa_{i,j+\frac{1}{2}} = \int_{\Omega_j}^{\Omega_{j+1}} g_i(\Omega) d\Omega$. To solve the integral value ρ and κ , we consider the Eq. (10) on given j and i grid respectively, and integrate it along ξ and Ω over the grid interval, which yields the time evolution of the integral values

$$\begin{aligned} \left. \frac{\partial \rho}{\partial t} \right|_{i+\frac{1}{2},j} &= \int_{\xi_i}^{\xi_{i+1}} [-m_j(\xi) \left. \frac{\partial g}{\partial \xi} \right|_j(\xi) + n_j(\xi) \left. \frac{\partial g}{\partial \Omega} \right|_j(\xi) + \mathcal{S}_j(\xi)] d\xi \\ \left. \frac{\partial \kappa}{\partial t} \right|_{i,j+\frac{1}{2}} &= \int_{\Omega_j}^{\Omega_{j+1}} [-m_i(\Omega) \left. \frac{\partial g}{\partial \xi} \right|_i(\Omega) + n_i(\Omega) \left. \frac{\partial g}{\partial \Omega} \right|_i(\Omega) + \mathcal{S}_i(\Omega)] d\Omega \end{aligned} \quad (16)$$

We apply the third-order central interpolation scheme to approximate the functions m and n along the ξ and Ω dimension and use the interpolating stencil again to approximate the

derivatives,

$$\begin{aligned}
\left. \frac{\partial g}{\partial \xi} \right|_j(\xi) &\simeq G\left(\xi; \left. \frac{\partial g}{\partial \xi} \right|_{i,j}, \left. \frac{\partial g}{\partial \xi} \right|_{i+1,j}, g_{i+1,j} - g_{i,j}\right) \\
\left. \frac{\partial g}{\partial \Omega} \right|_j(\xi) &\simeq G\left(\xi; \left. \frac{\partial g}{\partial \Omega} \right|_{i,j}, \left. \frac{\partial g}{\partial \Omega} \right|_{i+1,j}, \left. \frac{\partial \rho}{\partial \Omega} \right|_{i+\frac{1}{2},j}\right) \\
\left. \frac{\partial g}{\partial \Omega} \right|_i(\Omega) &\simeq G\left(\Omega; \left. \frac{\partial g}{\partial \Omega} \right|_{i,j}, \left. \frac{\partial g}{\partial \Omega} \right|_{i,j+1}, g_{i,j+1} - g_{i,j}\right) \\
\left. \frac{\partial g}{\partial \xi} \right|_i(\Omega) &\simeq G\left(\Omega; \left. \frac{\partial g}{\partial \xi} \right|_{i,j}, \left. \frac{\partial g}{\partial \xi} \right|_{i,j+1}, \left. \frac{\partial \kappa}{\partial \xi} \right|_{i,j+\frac{1}{2}}\right)
\end{aligned} \tag{17}$$

We apply additional interpolation functions to approximate the derivatives

$$\begin{aligned}
\left. \frac{\partial \rho}{\partial \Omega} \right|_{i+\frac{1}{2},j} &\simeq \left. \frac{\partial}{\partial \Omega} G(\Omega; \rho_{i+\frac{1}{2},j}, \rho_{i+\frac{1}{2},j+1}, M_{i+\frac{1}{2},j+\frac{1}{2}}) \right|_{i+\frac{1}{2},j}, \\
\left. \frac{\partial \kappa}{\partial \xi} \right|_{i,j+\frac{1}{2}} &\simeq \left. \frac{\partial}{\partial \xi} G(\xi; \kappa_{i,j+\frac{1}{2}}, \kappa_{i+1,j+\frac{1}{2}}, M_{i+\frac{1}{2},j+\frac{1}{2}}) \right|_{i,j+\frac{1}{2}},
\end{aligned} \tag{18}$$

where the surface integral $M_{i+\frac{1}{2},j+\frac{1}{2}} = \int_{\xi_i}^{\xi_{i+1}} \int_{\Omega_j}^{\Omega_{j+1}} g(t, \xi, \Omega) d\xi d\Omega$. The time evolution of this surface integral according to the Stokes theorem is given by

$$\begin{aligned}
\left. \frac{\partial M}{\partial t} \right|_{i+\frac{1}{2},j+\frac{1}{2}} &= \int_{\xi_i}^{\xi_{i+1}} n_{j+1}(\xi) g_{j+1}(\xi) d\xi - \int_{\Omega_j}^{\Omega_{j+1}} m_{i+1}(\Omega) g_{i+1}(\Omega) d\Omega \\
&\quad - \int_{\xi_i}^{\xi_{i+1}} n_j(\xi) g_j(\xi) d\xi + \int_{\Omega_j}^{\Omega_{j+1}} m_i(\Omega) g_i(\Omega) d\Omega \\
&\quad + \iint S(\xi, \Omega) d\xi d\Omega.
\end{aligned} \tag{19}$$

Here the integral of the source term is solved by trapezoidal integration. Equations (15), (16), and (19) are a set of ordinary differential equations that can be solved by Runge-Kutta (RK) method. For the boundary conditions, the distribution function in the resonant frame is assumed to be periodic in the phase angle ξ ,

$$g(\xi, \Omega, t) = g(\xi + 2\pi, \Omega, t). \tag{20}$$

Note that the periodicity only valid when the resonance not deviate too far from the initial resonance frame of reference given by the most unstable frequency ω_l and corresponding wave number k_l . The values of the perturbed distribution vanish at the Ω boundaries.

2.2. The Lagrangian step

For the Lagrangian markers, the sampling point for \mathcal{J} is chosen to ensure a uniform sampling to the initial equilibrium distribution f_0 ,

$$\mathcal{J}_l \rightarrow \int^{\mathcal{J}_l} f_0 d\mathcal{J} = l/N_l, \tag{21}$$

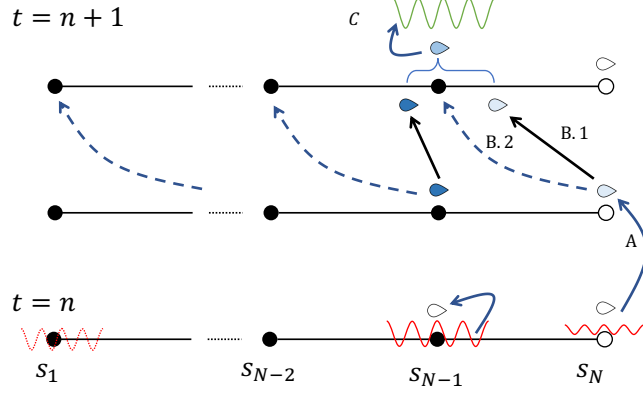


Figure 2: Schematic illustration of the hybrid Vlasov simulation scheme.

where N_l is the total number of sampling points for \mathcal{J} . An illustration is shown in Fig. 3(a).

To initially position the markers in the spatial domain, we place them on the fixed grid, denoted as s_i , which is the same grid used for solving the wave equations. To ensure that each marker updates over an identical time step, we implement nonuniform sampling, corresponding to the nonuniform wave grid. Initially, we calculate the transit time required for a marker to traverse the entire simulation domain.

$$T = \int_{s_1}^{s_N} \frac{ds}{v_r(s)} \quad (22)$$

where $v_r(s)$ is the local resonant velocity that has been predetermined from the background equilibrium parameter. Then the simulation time step is set as $\Delta t = T/N$ with N the total number of sampling points/grids. Finally the initial spatial coordinates of the markers are set according to equation (8) gives the trajectory of the Lagrangian marker.

$$s_{k+1} = s_k + \int_t^{t+\Delta t} v_r(s_k(t)) dt \quad (23)$$

where $k = 1, 2, 3, \dots, N$. The nonuniform grids with size Δs are shown in Fig. 3(b). Utilizing this nonuniform grid, the Lagrangian markers initially positioned on the grid advance to the next adjacent grid point after a time interval Δt . Thus we successively push the distribution $g_{k,l}(\xi, \Omega)$ from s_k to the next grid s_{k+1} for each time interval Δt . After pushing the Lagrangian marker from the n^{th} to the $n+1^{\text{th}}$ time step, the Hamiltonian is re-calculated by the equilibrium quantities at the new location of s and \mathcal{J} , which are needed for evolving the distribution in $\xi - \Omega$ space at the next time step.

To mitigate the checkboard numerical error, we also implement a uniform grid and sample Lagrangian markers on ' s ' to validate the effectiveness of our nonuniform grid approach. After a given time step Δt the markers deviated from the fixed grid, thus we need to interpolate the distribution function and its derivatives required in the IDO scheme from the

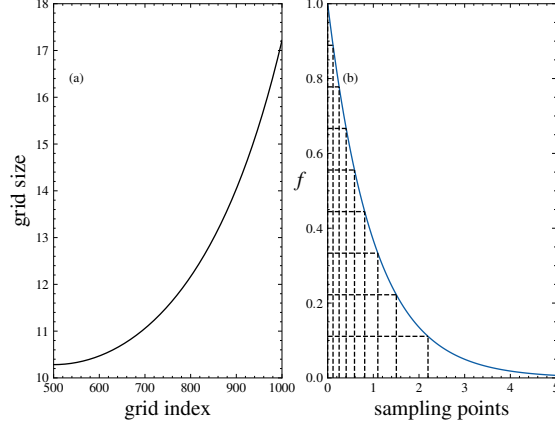


Figure 3: The nonuniform spatial grid obtained from resonance velocity.

adjacent marker to the fixed s grid. These procedures closely resemble those of the semi-Lagrangian method [22, 23]. Following interpolation, the markers realign with the grid, and the next iteration starts from the grid point. As shown in Fig. 4, the wave amplitudes calculated from the two approaches converge as the smaller grid sizes are used for the uniform grid with interpolation. The evolution of ϑ, \mathcal{J} in Eq. (9) are simply solved by applying the

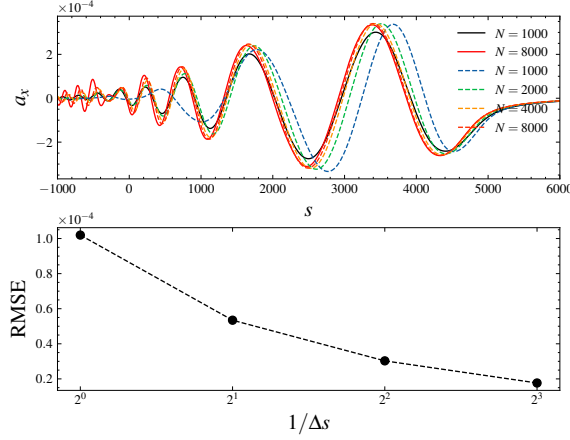


Figure 4: Wave amplitude from semi-Lagrangian method with linear interpolation of distribution at different uniform grid sizes (dashed-line) and the nonuniform grid (solid line).

RK method.

Given that the evolution in the ξ, Ω phase space occurs at a significantly faster pace compared to that in the s_i, \mathcal{J} domain, we employ a larger fixed time step Δt for the Lagrangian calculations. Conversely, we employ a much smaller adaptive time step, Δt_{adp} , for resolving the rapidly varying dynamics within the Eulerian domain. These Δt_{adp} are adaptively determined through real-time error analysis using the adaptive time step RK method, and satisfy

$$\sum_{t=1}^T \Delta t_{\text{adp}} = \Delta t . \quad (24)$$

where T is the total number of iterations within one Δt . As shown in Fig. 5, Δt_{adp} is continuously adjusted and refined, consistently reducing its value whenever the numerical error exceeds the predefined error threshold. As the system undergoes nonlinear evolution, the time step Δt_{adp} undergoes further refinement, automatically increasing the number of iterations within a single Δt interval. This highlights the clear advantage of adaptive hybrid methods in significantly improving computational efficiency.

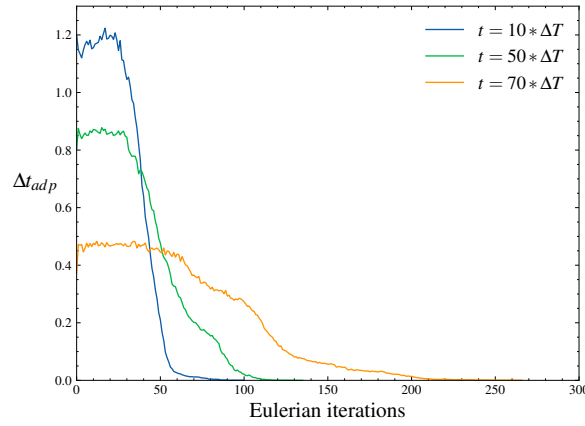


Figure 5: The variation of time step Δt_{adp} with the number of iterations for Eulerian calculation.

3. Wave Equation

We proceed to integrate the HEL Vlasov solver with the wave equation, enabling us to self-consistently investigate resonant wave-particle interactions. In this paper, we focus on the interaction between energetic electrons and chorus waves within the Earth's magnetosphere. Chorus waves are circularly polarized electromagnetic waves that propagate along the Earth's dipole magnetic field. The vector potential $\mathbf{A}(s, t)$ representing the transverse wave is expressed as follows:

$$\mathbf{A}(s, t) = \mathbf{a}(s, t)e^{i\phi_f} , \quad (25)$$

where ϕ_f is the fast varying phase and $\mathbf{a}(s, t)$ is the slowly varying envelope of the wave packet. The second order wave equation for the chorus in the resonant frame is

$$\begin{aligned} \frac{\partial^2 a}{\partial t^2} - \frac{\partial^2 a}{\partial s_i^2} + 2i\omega_l \frac{\partial a}{\partial t} + 2ik_l \frac{\partial a}{\partial s_i} + \\ \frac{\omega_p^2 \omega_{ce}}{(\omega_{ce} - \omega_l)} \int_0^t d\tau \frac{\partial a}{\partial \tau} e^{-i(\omega_l - \omega_{ce})(t - \tau)} = 4\pi j_p , \end{aligned} \quad (26)$$

where $a = a_x + \iota a_y$ with x and y the directions perpendicular to the magnetic field. The plasma current is a combination of contributions from both cold electrons and energetic electrons. The cold electron current can be analytically integrated. We represent the second-order wave equation (26) as a system of first-order ordinary differential equations, as shown below:

$$\begin{aligned}\frac{dy_0}{dt} &= y_1 + D \frac{\partial^2 y_0}{\partial s^2} \\ \frac{dy_1}{dt} &= -2\iota\omega_l y_1 + \frac{\partial^2 y_0}{\partial s^2} - 2\iota k_l \frac{\partial y_0}{\partial s} - \frac{\omega_p^2 \omega_{ce}}{\omega_{ce} - \omega_l} y_2 + j_p \\ \frac{dy_2}{dt} &= y_1 - \iota(\omega_l - \omega_{ce}) y_2 ,\end{aligned}\tag{27}$$

where we have added a numerical diffusive term with D the diffusive coefficient. The terms y_0, y_1 and y_2 are

$$\begin{aligned}y_0 &= a(s_i, t) , \\ y_1 &= \frac{\partial a(s_i, t)}{\partial t} , \\ y_2 &= e^{-\iota(\omega_l - \omega_{ce})t} \int_0^t d\tau \frac{\partial a}{\partial \tau} e^{\iota(\omega_l - \omega_{ce})\tau} .\end{aligned}\tag{28}$$

For the nonuniform, to ensure the order of precision, a linear combination of finite difference scheme is employed, and the first and second order spatial derivatives are given by

$$\frac{\partial f}{\partial z} \approx \frac{f(z_k) - f(z_{k-1})}{z_k - z_{k-1}} + \frac{f(z_k) - f(z_{k+1})}{z_k - z_{k+1}} - \frac{f(z_{k+1}) - f(z_{k-1})}{z_{k+1} - z_{k-1}} ,\tag{29}$$

and

$$\frac{\partial^2 f}{\partial z^2} \approx 2 \left(\frac{f(z_{k-1})}{(z_{k-1} - z_k)(z_{k-1} - z_{k+1})} + \frac{f(z_k)}{(z_k - z_{k+1})(z_k - z_{k-1})} + \frac{f(z_{k+1})}{(z_{k+1} - z_k)(z_{k+1} - z_{k-1})} \right) .\tag{30}$$

The energetic electron current j_p is obtained from the perpendicular velocity moment of energetic particle distribution,

$$j_p(s_i, t) = -\frac{n_{h0} k_l(t)}{4\pi} \iiint \sqrt{2m_e \omega_{ce}(s)(\mathcal{J} + \Omega + \Pi_i)} f e^{\iota \xi} d\xi d\Omega d\mathcal{J} ,\tag{31}$$

where n_{h0} is the density ratio of the energetic electrons to the background cold plasmas. The coupled ordinary differential equations (27) in terms of time are subsequently resolved using the RK method.

To check the contribution of the second order derivatives of slowly varying kernel $a(s_i, t)$ in the wave equation (26), we further simplify the integral term and obtain the first-order advective wave equation

$$\frac{\partial a}{\partial t} + v_g^l \frac{\partial a}{\partial s_i} = \frac{2\pi v_g^l}{k_l} j_p ,\tag{32}$$

where v_g^l is the linear group velocity.

$$a_k^{n+1} = \left[S_k^n \pm \frac{\text{imp}}{\Delta s} u_k a_{k\pm 1}^{n+1} + \left(\frac{1}{\Delta t} - \frac{(1 - \text{imp})}{\Delta s} u_k \right) a_k^n \pm \frac{(1 - \text{imp})}{\Delta s} u_k a_{k\pm 1}^n \right] / \left(\frac{1}{\Delta s} + \frac{\text{imp}}{\Delta s} u_k \right) \quad (33)$$

where $u_k = v_g(s = s_k)$, S_k is the source term in the right-hand-side of Eq. (32), **imp** is the combination factor of the implicit-explicit upwind scheme. The sign of the advective term depends on the direction of the group velocity. We apply absorption boundary conditions at one end of the domain and a fixed noisy initialization condition at the other end.

Fig. 6 demonstrates that the first-order wave equation provides a strong approximation to the second-order wave equation. Consequently, the second-order term in Eq. (26) may be disregarded when simulating the onset of chorus wave frequency chirping for the sake of computational efficiency.

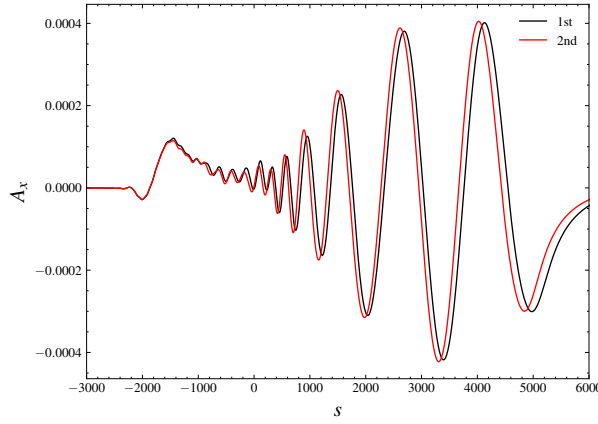


Figure 6: Wave amplitudes calculated from the second-order and first-order wave equations.

4. Benchmark Results for the Onset of Rising Tone Chorus

We proceed with a series of simulations, employing our method to investigate the initiation of the whistler-mode chorus. The instability of the whistler wave typically arises from the electron temperature anisotropy instability [24, 25], and the growth rate can be derived from the linear resonance condition near $\Omega \approx 0$.

In our simulation, the energetic electron distribution is bi-Maxwellian at the magnetic equator. Moving away from the magnetic equator, the equilibrium distribution maintains the similar form as it does in the phase space by conventional coordinates $(s_i, p_{\parallel}, \phi, \varphi)$. The distribution function in new canonical variables is given directly by canonical transformation in ref [1], and we have

$$f_0(\Omega, \mathcal{J}) = \frac{\omega_{ce0}}{(2\pi)^{3/2} v_{th\perp 0}^2 v_{th\parallel 0}} \frac{1}{1 - \beta} \cdot \exp\left(-\frac{k_{\perp}^2 (\Omega + \Pi_i)^2}{2v_{th\parallel 0}^2}\right) \cdot \left(\exp\left(-\frac{(\mathcal{J} + \Omega + \Pi_i)\omega_{ce0}}{v_{th\perp 0}^2}\right) - \exp\left(-\frac{(\mathcal{J} + \Omega + \Pi_i)\omega_{ce0}}{\beta v_{th\perp 0}^2}\right) \right), \quad (34)$$

Table 1: Magnetic field and plasma parameters used in the simulation.

L-shell of the magnetic field line	5
Magnetic field inhomogeneity ratio R_a	4.5
Background cold plasma density inhomogeneity ratio R_b	1.0
Background electron gyro frequency and plasma frequency	$\omega_{ce} = 0.2$ $\omega_{pe} = 1$
Density ratio between energetic and cold electrons at the magnetic equator	0.002
Parallel and perpendicular thermal velocity of energetic electrons	$v_{\perp} = 0.3c$ $v_{\parallel} = 0.15c$
Depth of the loss cone β	0
Size of the simulation domain	$\lambda \in [-15^\circ, 15^\circ]$ $s \in [-6115, 6115]c/\omega_{pe}$

where β is the depth of the loss cone, the subscript 0 denotes the magnetic equator.

As a realistic model for the magnetosphere, the magnetic field can be approximated as a dipole field, and the major component of the background magnetic field near the equator can be approximately represented by a parabolic function [26]

$$B(\lambda) = B_0(1 + R_a\lambda^2), \quad (35)$$

where R_a is the inhomogeneity ratio of the magnetic field, B_0 is the magnetic field strength at the equator, and λ is the magnetic latitude. The distance along the magnetic field line s satisfies $s = LR_E\lambda$. The background electron density is found to fit a power law form [27],

$$n(\lambda) = n_0(1 + R_b\lambda^2) \quad (36)$$

where R_b is a fitting parameter in an order of one.

4.1. Simulation configuration

In conventional PIC simulations, the inhomogeneity ratio R_a was often enlarged by one or two order of magnitudes to reduce the simulation cost. However, one of the advantages of our numerical scheme is that we can use realistic parameters for the Earth's dipole field. The basic parameters of our simulation are given in Tab. (4.1). The profile of the background parameter is shown in Fig. 7. Meanwhile, we show the most unstable wave frequency applied in the simulation for the determination of initial reference frame. According to the chosen parameter in Tab. (4.1) and the definition of growth rate γ_l at the equator

$$\gamma_l(s) = \frac{\sqrt{2\pi}\omega_{ce}v_g\omega_{h0}^2}{4k_l^2v_{th||0}} e^{-\frac{(\omega_l - \omega_{ce})^2}{2k_l^2v_{th||0}}} \cdot \left((1 + \beta) \frac{T_{\perp 0}}{T_{||0}} \frac{\omega_{ce0} - \omega_l}{\omega_{ce0}} - 1 \right) \quad (37)$$

The most unstable frequency is $\omega_l = 0.061$ and the corresponding growth rate is $\gamma_l \approx 3.24 \times 10^{-4}$, as shown by a scan of the parameter given in Fig. 8.

Benefiting from the scale-separated numerical scheme we set the number of grids for wave solver to 1001, aligning it with the number of sampling points in s . In the \mathcal{J} dimension, we

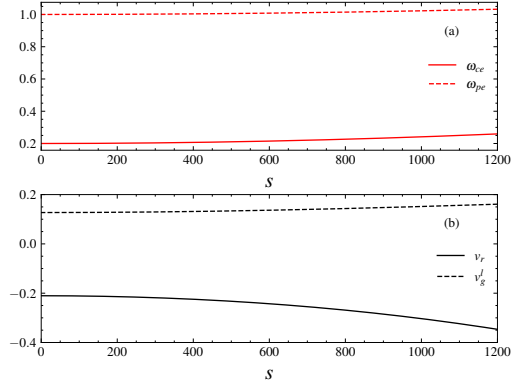


Figure 7: (a) Background magnetic field and density profile. (b) Characteristic velocity in our simulation.

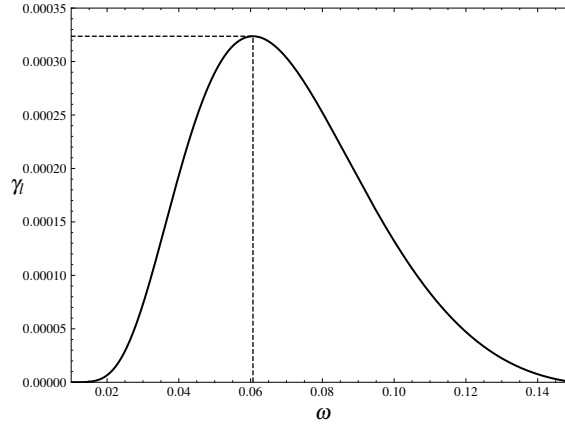


Figure 8: Linear growth rate γ with respect to ω in the chosen parameter. The initial frequency of the wave is obtained from the most unstable frequency indicated by the vertical black line.

employ a delta function, necessitating only a single sampling point for \mathcal{J} . In the case of a non-delta distribution, tens of sampling points prove sufficient for \mathcal{J} sampling. As to the ξ, Ω domain, the Eulerian grids are 31×401 for $\xi \in [0, 2\pi]$ and $\Omega \in [-0.1, 0.1]$.

The wave is resolved within a reduced-dimensional space, leading to a relatively manageable workload, as is the case with the Lagrangian solver. However, the bottleneck occurs within the Eulerian solver, primarily due to its two-dimensional space, necessitating hundreds of iterations for a single Lagrangian time step for all markers. Nonetheless, the computational cost remains reasonable in comparison to conventional PIC simulations, where the number of sampling points is at least several orders of magnitude greater than in our method. Consequently, their simulations require several billion particles [28, 29], but the phase space resolution is significantly lower than ours.

4.2. Benchmarks results

The linear physics are quantitatively verified in Fig. 9, where we calculate the growth rate and the velocity of the maximum wave amplitude location before nonlinear effects become dominant. In the case of the propagating wave, we determine the trajectory of the wave packet using the integral of the group velocity,

$$s(t) = s(0) + \int_0^t v_g(s(\tau)) d\tau. \quad (38)$$

Here we trace the movement of the maximum amplitude point. Its propagation is in accord with the linear group velocity, as shown in Fig. 9(a). For the wave peak, it indeed propagates in the linear group velocity during the linear stage. Moreover, we estimate the amplitude growth of the wave peak along its propagation path, the growth rate is given by [28]

$$\Gamma = \frac{1}{t_1 - t_0} \log \frac{|a(s_1, t_1)|}{|a(s_0, t_0)|}, \quad (39)$$

where s_0, t_0, s_1, t_1 are along the propagation path. The growth of the amplitude along the propagation path is shown in Fig. 9(b). The corresponding growth rate from equation (39) is $\Gamma_0 \simeq 3.21 \times 10^{-4}$, agrees well with the theoretic linear growth rate shown in Fig. 8. The results show the correctness of our simulation at linear stage.

In the nonlinear stage, trapped electrons form a phase space hole in $\xi - \Omega$. This phase space hole contributes to the nonlinear current, which in turn triggers the nonlinear frequency-chirping chorus wave [30]. The shape of the hole, specifically its boundary, can be analytically described as follows:

$$\Omega(\xi) = \pm \frac{\omega_b}{k^2} \sqrt{2(e_{spx} - \cos \xi - \alpha \xi)} \quad (40)$$

where e_{spx} is the particle energy on the separatrix, k is the wave number and $\omega_b \equiv \sqrt{k^2 v_{\perp} a}$ is the trapped particle bounce frequency. The parameter is the inhomogeneity ratio [30, 31]

$$\alpha \equiv \frac{1}{\omega_b^2} \left[\left(1 - 2 \frac{v_r}{v_g} \right) \frac{\partial \omega}{\partial t} - v_r^2 \frac{\partial k}{\partial s} + \frac{\partial \omega_{ce}}{\partial s} \frac{k_i}{m_e} \mathcal{J} \right]. \quad (41)$$

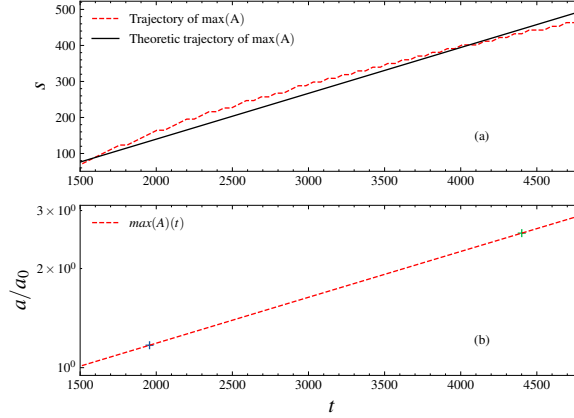


Figure 9: Figure (a) is the propagation velocity of the linear wave packet with the maximum amplitude. Figure (b) denotes the growth of the wave peak amplitude with time along wave propagation path. The green cross marks the point used to calculate the growth rate.

In Fig. 10, we present a typical electron phase-space hole observed at a specific location s in the late nonlinear stage. We determined the corresponding values of $k \simeq 0.649$, $\omega_b \simeq 0.007$, $\alpha \simeq 0.08$ based on the simulation data at that location. Additionally, we illustrated the boundary of the hole using the equation (40). Notably, the shape of the hole closely aligns with the theoretical predictions.

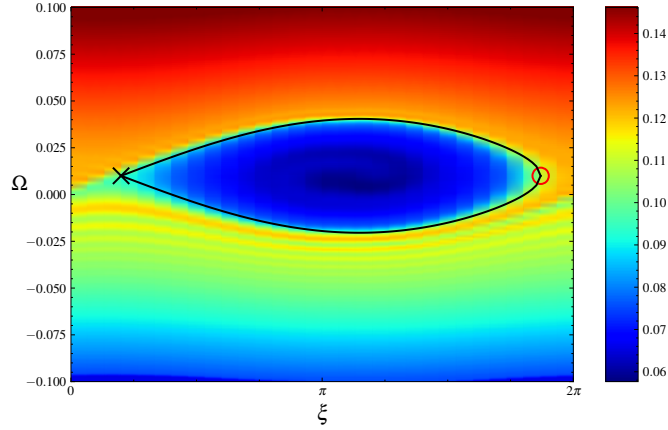


Figure 10: Phase-space hole formed by trapped electrons in the wave field. The size and location of the hole, i.e., the X, C points, and the boundary, are determined from the nonlinear theory.

5. Conclusion

In summary, we have developed a hybrid Lagrangian-Eulerian method tailored for the resonance tracking Vlasov system. This method effectively segregates the perturbed wave-particle interactions within the fast-varying Hamiltonian phase space, while simultaneously

advancing Lagrangian markers within the slowly varying Hamiltonian phase space. To validate its efficacy, we conducted several simulations focusing on the whistler mode chorus in the Earth’s magnetosphere. The results not only exhibit strong agreement with prior findings but also offer a higher-resolution portrayal of the resonant particle phase space. The implications of this research are profound, spanning a spectrum of scientific disciplines, including fusion research, space physics, and astrophysics. This advancement in our understanding of nonlinear wave-particle interactions within inhomogeneous magnetic fields holds the potential to revolutionize our capacity to control and manipulate plasma behavior. This, in turn, can pave the way for progress in energy generation, propulsion, and space exploration. Thus, this paper represents a pivotal milestone in unlocking the untapped potential of nonlinear plasma physics within complex magnetic field environments.

References

- [1] L. Chen, F. Zonca, Physics of Alfvén waves and energetic particles in burning plasmas, *Rev. Mod. Phys.* 88 (2016) 72.
- [2] G. Wang, H. Berk, B. Breizman, L.-J. Zheng, Frequency chirping in the Alfvén continuum, *Nuclear Fusion* 58 (2018) 082014.
- [3] A. Fasoli, C. Gormenzano, H. L. Berk, B. Breizman, S. Briguglio, D. S. Darrow, N. Gorelenkov, W. W. Heidbrink, A. Jaun, S. V. Konovalov, R. Nazikian, J.-M. Noterdaeme, S. Sharapov, K. Shinohara, D. Testa, K. Tobita, Y. Todo, G. Vlad, F. Zonca, Chapter 5: Physics of energetic ions, *Nuclear Fusion* 47 (2007) S264–S284.
- [4] B. T. Tsurutani, E. J. Smith, Postmidnight chorus: A substorm phenomenon, *Journal of Geophysical Research* (1896-1977) 79 (1974) 118–127.
- [5] B. Van Compernelle, X. An, J. Bortnik, R. M. Thorne, P. Pribyl, W. Gekelman, Excitation of Chirping Whistler Waves in a Laboratory Plasma, *Physical Review Letters* 114 (2015) 245002.
- [6] B. Van Compernelle, X. An, J. Bortnik, R. M. Thorne, P. Pribyl, W. Gekelman, Laboratory simulation of magnetospheric chorus wave generation, *Plasma Physics and Controlled Fusion* 59 (2017) 014016.
- [7] S. Kasahara, Y. Miyoshi, S. Yokota, T. Mitani, Y. Kasahara, S. Matsuda, A. Kumamoto, A. Matsuoka, Y. Kazama, H. U. Frey, V. Angelopoulos, S. Kurita, K. Keika, K. Seki, I. Shinohara, Pulsating aurora from electron scattering by chorus waves, *Nature* 554 (2018) 337–340.
- [8] G. D. Reeves, H. E. Spence, M. G. Henderson, S. K. Morley, R. H. W. Friedel, H. O. Funsten, D. N. Baker, S. G. Kanekal, J. B. Blake, J. F. Fennell, S. G. Claudepierre, R. M. Thorne, D. L. Turner, C. A. Kletzing, W. S. Kurth, B. A. Larsen, J. T. Niehof, Electron Acceleration in the Heart of the Van Allen Radiation Belts, *Science* 341 (2013) 991–994.
- [9] R. M. Thorne, W. Li, B. Ni, Q. Ma, J. Bortnik, L. Chen, D. N. Baker, H. E. Spence, G. D. Reeves, M. G. Henderson, C. A. Kletzing, W. S. Kurth, G. B. Hospodarsky, J. B. Blake, J. F. Fennell, S. G. Claudepierre, S. G. Kanekal, Rapid local acceleration of relativistic radiation-belt electrons by magnetospheric chorus, *Nature* 504 (2013) 411–414.
- [10] M. K. Lilley, B. N. Breizman, S. E. Sharapov, Destabilizing Effect of Dynamical Friction on Fast-Particle-Driven Waves in a Near-Threshold Nonlinear Regime, *Physical Review Letters* 102 (2009) 195003.
- [11] B. N. Breizman, Nonlinear travelling waves in energetic particle phase space, *Nuclear Fusion* 50 (2010) 084014.
- [12] H. Hezaveh, Z. Qu, B. Layden, M. Hole, Impact of energetic particle orbits on long range frequency chirping of BGK modes, *Nuclear Fusion* 57 (2017) 126010.
- [13] H. Hezaveh, Z. S. Qu, B. N. Breizman, M. J. Hole, Long range frequency chirping of Alfvén eigenmodes, *Nuclear Fusion* 60 (2020) 056014.

- [14] H. Hezaveh, Z. S. Qu, M. J. Hole, R. L. Dewar, Theoretical description of chirping waves using phase-space waterbags, *Plasma Physics and Controlled Fusion* 63 (2021) 065008.
- [15] C. M. Bender, S. A. Orszag, *Advanced Mathematical Methods for Scientists and Engineers I*, Springer New York, New York, NY, 1999. URL: <http://link.springer.com/10.1007/978-1-4757-3069-2>. doi:10.1007/978-1-4757-3069-2.
- [16] F. Arecchi, R. Bonifacio, Theory of optical maser amplifiers, *IEEE Journal of Quantum Electronics* 1 (1965) 169–178.
- [17] V. I. Karpman, J. N. Istomin, D. R. Shklyar, Nonlinear theory of a quasi-monochromatic whistler mode packet in inhomogeneous plasma, *Plasma Physics* 16 (1974) 685–703.
- [18] N. Bleistein, R. A. Handelsman, *Asymptotic Expansions of Integrals*, Dover Publications, New York, 1986.
- [19] V. Guillemin, S. Sternberg, *Geometric Asymptotics*, volume 14 of *Mathematical Surveys and Monographs*, revised ed., American Mathematical Society, Providence, Rhode Island, 1977. URL: <http://www.ams.org/surv/014>. doi:10.1090/surv/014.
- [20] T. Shiroto, A. Matsuyama, M. Yagi, A charge-momentum-energy-conserving 1D3V hybrid Lagrangian–Eulerian method for Vlasov–Maxwell system, *Journal of Computational Physics* 469 (2022) 111522.
- [21] K. Imadera, Y. Kishimoto, D. Saito, J. Li, T. Utsumi, A numerical method for solving the Vlasov–Poisson equation based on the conservative IDO scheme, *Journal of Computational Physics* 228 (2009) 8919–8943.
- [22] E. Sonnendrücker, J. Roche, P. Bertrand, A. Ghizzo, The Semi-Lagrangian Method for the Numerical Resolution of the Vlasov Equation, *Journal of Computational Physics* 149 (1999) 201–220.
- [23] G.-H. Cottet, Semi-Lagrangian particle methods for high-dimensional Vlasov–Poisson systems, *Journal of Computational Physics* 365 (2018) 362–375.
- [24] C. F. Kennel, H. E. Petschek, Limit on stably trapped particle fluxes, *Journal of Geophysical Research* 71 (1966) 1–28.
- [25] C. F. Kennel, Velocity Space Diffusion from Weak Plasma Turbulence in a Magnetic Field, *Physics of Fluids* 9 (1966) 2377.
- [26] X. Tao, A numerical study of chorus generation and the related variation of wave intensity using the DAWN code, *Journal of Geophysical Research: Space Physics* 119 (2014) 3362–3372.
- [27] R. E. Denton, Electron density in the magnetosphere, *J. Geophys. Res.* 109 (2004) A09215.
- [28] T. Nogi, Y. Omura, Nonlinear Signatures of VLF-Triggered Emissions: A Simulation Study, *JGR Space Physics* 127 (2022) e2021JA029826.
- [29] Y. Katoh, Y. Omura, Electron hybrid code simulation of whistler-mode chorus generation with real parameters in the Earth’s inner magnetosphere, *Earth, Planets and Space* 68 (2016) 192.
- [30] Y. Omura, Y. Katoh, D. Summers, Theory and simulation of the generation of whistler-mode chorus, *J. Geophys. Res. Space Phys.* 113 (2008).
- [31] X. Tao, F. Zonca, L. Chen, Y. Wu, Theoretical and numerical studies of chorus waves: A review, *Science China Earth Sciences* 63 (2020) 78–92.